



Construction of Z-type heterojunction BiVO₄/Sm/ α -Fe₂O₃ photoanode for selective degradation: Efficient removal of bisphenol A based on multifunctional Sm-doped modification

Yiran Chen^a, Lu Liu^a, Lu Zhang^a, Shunlin Li^a, Xinyu Zhang^a, Wenchao Yu^a, Feng Wang^b, Wanlai Xue^c, Hui Wang^{a,*}, Zhaoyong Bian^{b,**}

^a College of Environmental Science and Engineering, Beijing Forestry University, Beijing 100083, PR China

^b College of Water Sciences, Beijing Normal University, Beijing 100875, PR China

^c Beijing Water Science and Technology Institute, Beijing 100048, PR China

ARTICLE INFO

Keywords:

Photoanode
Extended light response
Charge transfer acceleration
Sm photosensitizer
Bisphenol A

ABSTRACT

Metal Sm was doped in the BiVO₄ to form B-Sm, and then B-Sm is combined with α -Fe₂O₃ to form B-Sm/ α -Fe₂O₃ Z-type heterojunction to determine the mechanism of Sm in the photoanode heterojunction and oxidation system for lanthanide metal application in water treatment. In the photoanode mechanism, Sm utilizes near-infrared light at 980 nm to increase the light absorption intensity at 400–500 nm. It also decreases the transmission resistance from 25.91 Ω to 20.47 Ω , increases the number of oxygen vacancies in the system, and improves the carrier life and conductivity of the photoanode. In the oxidation system, the metal Sm acts as a photosensitizer to convert the O₂ adsorbed on oxygen vacancies to ¹O₂, which increases the degradation rate of bisphenol A by 36%. Finally, the B-Sm-F photoanode was able to achieve 100% degradation within 60 min. Furthermore, the DFT results showed that the active species were selectively aggressive towards different sites of the bisphenol analogues. This provides a pathway for the selective degradation of bisphenol analogues.

1. Introduction

With the development of society and industry, a large amount of endocrine disruptors (EED) are continuously released from human life and the corresponding production processes, resulting in the widespread presence of EEDs in sewage, surface water, sediments, groundwater and even drinking water. EED pollution has attracted extensive attention worldwide [1]. Among them, the wide application of the plasticizer bisphenol A (2,2-bisphenol propane, BPA) leads to its prevalence in water, air, and soil [2,3]. As a typical endocrine disruptor, bisphenol A has been fully proven to cause adverse effects in organisms and humans, such as induced breast tumours and obesity, brain changes and immune system damage [4]. In recent years, photoelectrocatalytic technology has become an effective means of eliminating environmental pollutants due to its low energy consumption and remarkable effects [5]. Among these technologies, BiVO₄ has become a common semiconductor in the photoelectrocatalytic field because of its suitable band gap width and

low preparation cost. Moreover, BiVO₄ photoanodes have been found to have good degradation effects on BPA in many studies [6,7]. Therefore, BiVO₄-based photoelectrocatalysis has broad application prospects in the degradation of bisphenol refractory organic compounds.

Rare earth (RE) ions have good application prospects due to their three advantages, but their application mechanism in photoelectrocatalysis is not clear. Initially, rare earth ions have complex 4f energy levels, which can introduce energy impurity levels to promote charge separation and electron transfer between heterojunctions [8]. Then, it has a unique upconversion luminescence effect, which can effectively improve the light absorption performance of its semiconductor in the visible range [9,10]. The Nd/Er codoped tetragonal BiVO₄ greatly improved its oxidation ability and effectively degraded rhodamine B within 20 min by using the near-infrared radiation band [11]. Metal Y increased the light absorption range of BiVO₄, and the maximum degradation rates of MB, MO and RhB within 180 min were 93%, 85% and 91%, respectively [12]. Finally, lanthanide metals can

* Correspondence to: College of Environmental Science and Engineering, Beijing Forestry University, PO Box 60, No. 35 Qinghua East Road, Haidian District, Beijing 100083, PR China.

** Correspondence to: College of Water Sciences, Beijing Normal University, No. 19 XinJieKouWai Street, Haidian District, Beijing 100875, PR China.

E-mail addresses: wanghui@bjfu.edu.cn (H. Wang), bian@bnu.edu.cn (Z. Bian).

<https://doi.org/10.1016/j.apcatb.2023.122775>

Received 24 October 2022; Received in revised form 27 March 2023; Accepted 17 April 2023

Available online 18 April 2023

0926-3373/© 2023 Elsevier B.V. All rights reserved.

also well control the crystal phase of BiVO_4 and adjust the activity of the catalyst [13]. However, the application mechanism of rare earth elements in the field of photoelectrocatalysis is not very clear. Sm mainly changes the electronic band structure of BiVO_4 to improve the oxidation performance of the photoanode [14]. However, the formation of internal energy states of rare earth metals reduces the recombination rate of photoexcited electron-hole pairs and improves the photoelectrochemical water splitting ability [12]. Therefore, it is particularly necessary to explore the application mechanism of rare earth in photoelectrochemical (PEC) systems.

According to previous studies, monoclinic BiVO_4 is a narrow band gap semiconductor (approximately 2.4 eV), and its electrons and holes are very easy to compound [6,7,11]. Therefore, constructing heterojunctions and enhancing their electron-hole separation effects through charge transfer have become common modification methods. Ultra-thin iron oxide films can minimize the charge carrier recombination in BiVO_4 [52]. The n-n isotype heterojunction composed of the two semiconductors is better than the original BiVO_4 anode in terms of both photoanode performance and degradation performance [15]. However, the Z-scheme $\text{Fe}_2\text{O}_3/\text{BiVO}_4$ photocatalyst can effectively reduce a variety of aromatic nitro compounds to the corresponding aniline [16]. Therefore, no consistent conclusion has been reached regarding the mechanism of heterojunction formation between two semiconductors, and its structural type is worth exploring.

In this study, the metal Sm can be doped in BiVO_4 to form B-Sm catalyst, and then B-Sm and $\alpha\text{-Fe}_2\text{O}_3$ to form B-Sm-F catalyst, which explores the mechanism of metal Sm in the PEC system. In addition, the degradation pathway of bisphenol A was evaluated by high-performance liquid chromatography–mass spectrometry (HPLC–MS) and density functional theory (DFT) calculations, and the bond-breaking mode of bisphenol analogues was explored by DFT.

2. Materials and methods

2.1. Materials

$\text{Bi}(\text{NO}_3)_3 \cdot 5\text{H}_2\text{O}$, NH_4VO_3 , oxalic acid ($\text{C}_2\text{H}_2\text{O}_4$), $\text{Sm}(\text{NO}_3)_3 \cdot 6\text{H}_2\text{O}$, $\text{Fe}(\text{NO}_3)_3 \cdot 9\text{H}_2\text{O}$, NaOH and other analytical pure reagents were purchased from Shanghai McLean Biochemical Co., Ltd. and were used without further purification. Fluorine-doped tin oxide (FTO, $< 15 \Omega/\text{sq}$) conductive glass was selected from Japan Plate Glass Co., Ltd., Before the experiment, all FTO substrates were washed with deionized water, ethanol, and acetone in a certain order (precut: $2 \text{ cm} \times 3 \text{ cm}$) for 15 min by ultrasonic cleaning.

2.2. Fabrication of photoanodes

2.2.1. BiVO_4/FTO photoanode

First, 5 mmol of $\text{Bi}(\text{NO}_3)_3 \cdot 5\text{H}_2\text{O}$ was added to 0.1 mol/L of oxalic acid solution and stirred at room temperature to obtain precursor A. At the same time, NH_4VO_3 with the corresponding molar amount was added to 60 mL of deionized water and stirred. The product was named precursor B. Then, precursor B was added to precursor A and stirred. The pH of the solution was adjusted with NaOH solution and transferred to a hydrothermal reactor. The reaction was performed at 180°C for 6 h, cooled to room temperature, and the yellow precipitate was collected, washed with distilled water and anhydrous ethanol, and dried to obtain the final product, namely, BiVO_4 . The product was then electrodeposited on FTO with a stable voltage of 35 V and a deposition time of 5 min [17, 18].

2.2.2. B-Sm/FTO photoanode

On the basis of the above preparation of BiVO_4 , $\text{Sm}(\text{NO}_3)_3 \cdot 6\text{H}_2\text{O}$ was added into the above mixture after adjusting the pH value. After stirring for 30 min, the mixture was transferred to a 100 mL hydrothermal kettle and reacted at the screening temperature for the screening time. The

obtained samples were washed three times alternately with deionized water and anhydrous ethanol and then dried at 60°C for 10 h. The sample was placed in a tube furnace and annealed at 300°C for 2 h. Then, under the same conditions, the B-Sm catalyst was electrodeposited on FTO. B-Sm2 denotes 2 wt% Sm doped in BiVO_4 , B-Sm4 denotes BiVO_4 doped with 4 wt% Sm, B-Sm8 denotes BiVO_4 doped with 8 wt% Sm (Table S1).

2.2.3. B-Sm-F/FTO photoanode

Five grams of $\text{Fe}(\text{NO}_3)_3 \cdot 9\text{H}_2\text{O}$ was dissolved in 70 mL of deionized water [19], adjusted to pH=13 with NaOH, hydrothermally treated at 180°C for 2 h, and dried in an oven. Then, $\alpha\text{-Fe}_2\text{O}_3$ was obtained by burning the above mixture in a tube furnace at 400°C for 2 h. Then, it was electrodeposited on B-Sm/FTO and sintered at 300°C in a tube furnace. The composite electrode was named B-Sm-F/FTO. The preparation process is shown in Scheme 1. The specific composition of the photoanode is shown in Table S1.

2.3. Characterization

The surface morphology of the material was investigated by scanning electron microscopy (SEM, Hitachi S-4800, Japan). Transmission electron microscopy (TEM, Tecnai G2Tf20 transmission electron microscopy 200kV) and energy dispersive spectrometer (EDS) elemental spectroscopy (TEM ring dark field detector study) were used to explore the structure and surface element composition of the heterojunction interface. X-ray diffraction (XRD, Shimadzu, Japan) was used to determine the crystal structure of the catalyst by employing an X'Pert PRO MPD diffractometer and $\text{CuK}\alpha$ radiation source. Photoelectron spectroscopy (PHI5300 Perkin Elmer, USA) was used to determine the valence state of the catalyst. With BaSO_4 as the reference, the optical absorption capacity and band gap of the sample were determined by UV–Vis absorption spectroscopy (U-2910), using BaSO_4 as the reference. Photoluminescence (PL) spectra were measured by a Hitachi F-7000 spectrophotometer. The adsorption-desorption isothermal curve and pore size were measured by the American Mike BET adsorption-desorption instrument ASAP2460. The up-converting photoluminescence spectra (UCPL) were measured by a steady-state transient fluorescence spectrometer (Edinburgh FLS-9800). The time-resolution photoluminescence spectrum (TRPL) was measured by a steady-state transient fluorescence spectrometer (Edinburgh FLS-1000). The ultra-violet photo-electron spectroscopy (UPS) (the valence band position and power functions) was measured by a photoelectron spectrometer (Thermo ESCALAB 250XI).

2.4. PEC measurements

All PEC tests were completed using an electrochemical workstation (CH Instruments Co., Ltd., CHI 660d, USA), and a 350 W xenon lamp (Shanghai Hualun Bulb Factory) was used as the simulated sunlight source. In a 1 mol/L NaOH and 1 mol/L Na_2SO_3 (pH=13) electrolyte solution, the linear sweep voltammetry (LSV) of the photoelectrode was measured using a three-electrode system with a platinum foil counter electrode, Ag/AgCl reference electrode and the prepared photoelectrode working electrode. The Mott-Schottky, cyclic voltammetry (CV), electrochemical impedance spectroscopy (EIS) (1.23 V vs RHE) and open circuit photovoltage (OCP) were measured in 1 mol/L NaOH solution. The time-current curve (I-T) was measured in 1.23 V vs RHE and 1 mol/L NaOH solution. The potential between Ag/AgCl and the standard hydrogen electrode is converted by using the Nernst formula [20].

2.5. Degradation measurement of BPA

The degradation experiment of the organic compound BPA was carried out under the following conditions: medium stirring, bias voltage, and 0.1 mol/L sodium sulfate electrolyte. The device is shown

in Scheme 2. All BPA degradation experiments were carried out in 50 mL of continuously stirred aqueous solution with a contaminant concentration of 20 mg/L. To avoid experimental errors, two parallel experiments were performed in each group. The BPA solution concentration was measured by high-performance liquid chromatography (HPLC) (ODS-S C18 liquid chromatography column). The HPLC–MS samples were mixed with standard substances for 0 min, 60 min and 120 min. Degradation reaction products were analysed using a Dionex UltiMate 3000 UHPLC system connected to a Thermo Q-Exactive Plus mass spectrometer (Thermo Fisher Scientific, USA) in 1 ESI+/- mode using Column C18. Hydroxyl radicals ($\cdot\text{OH}$) and superoxide anions ($\cdot\text{O}_2^-$) were captured by 5,5-dimethyl-1-pyrroline-N-oxide (DMPO). The singlet oxygen ($^1\text{O}_2$) was captured by 2,2,6,6-tetramethylpiperidine oxide (TEMPO), and the results were determined by an electron spin resonance (ESR, Bruker EMXPLUS10/12) instrument. In the quenching experiment, furfuryl alcohol (FFA) quenched $^1\text{O}_2$, tert-butyl alcohol (TBA) quenched $\cdot\text{OH}$, EDTA-2Na quenched h^+ , and hydroquinone (BQ) quenched O_2^- [22].

2.6. DFT calculation

The Fukui function is a very important concept in conceptual density functional theory, and it has been widely used in the prediction of reactive sites. The molecular structure optimization and frontier orbital calculation of BPA were performed using the B3LYP/6-31 G (d, p) basis set in DFT. The Fukui function [23] and dual descriptors [24] were used to calculate the Hirshfield charge of the BPA molecule with Multiwfn 3.7 software and then the electrophilic attack index (f^-), nucleophilic attack index (f^+), free radical attack index (f^0) and dual descriptors (Δf) were calculated using the following formula. The Fukui function is defined as shown in Eqs. (1)–(4):

$$f^+ = q_{N+1} - q_N \quad (1)$$

$$f^- = q_N - q_{N-1} \quad (2)$$

$$f^0 = (f^+ + f^-)/2 \quad (3)$$

$$\Delta f = f^+ - f^- \quad (4)$$

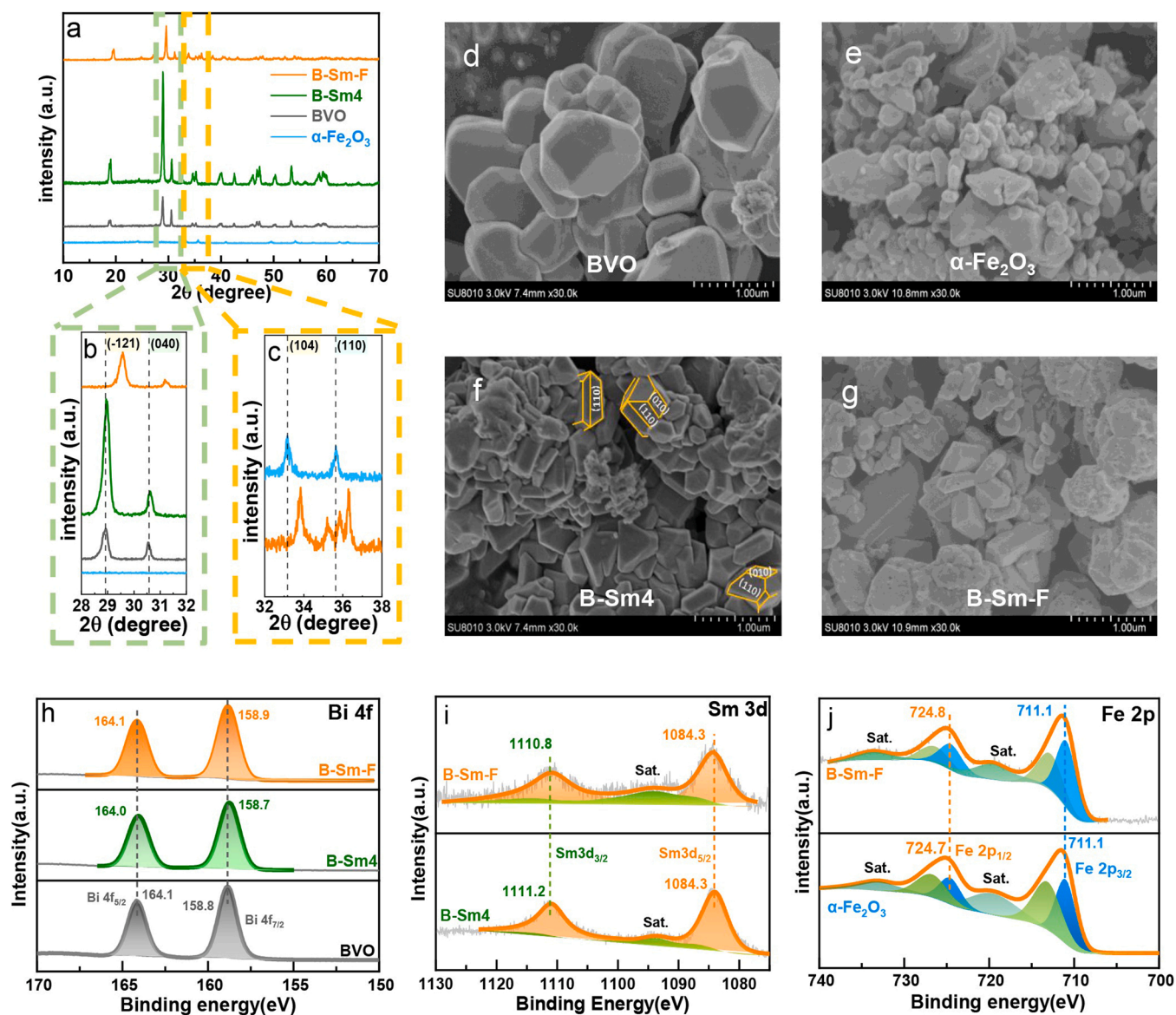


Fig. 1. XRD patterns for (a) 10° – 70°; (b) 28° – 32°; (c) 10° – 70° for α-Fe₂O₃ and B-Sm-F; SEM for 1 μm of (d) BiVO₄, (e) B-Sm4, (f) α-Fe₂O₃ and (g) B-Sm-F; XPS spectra for (h) Bi 4f, (i) Sm 3d, and (j) Fe 2p.

3. Results and discussion

3.1. Microstructure of the photoelectric catalyst

To study the crystal structure properties of the catalyst, XRD and XPS of the photoanode were performed, as shown in Fig. 1. Fig. 1a shows that BiVO_4 , B-Sm4 and B-Sm-F are monoclinic scheelite structures (JADE No. 14-0688). No significant differences between the XRD patterns of B-Sm2 and BiVO_4 are observed (Fig. S1). 4 wt% metal Sm doping does not change the crystal form of BiVO_4 (Fig. 1a), and there is no relative peak of metal Sm due to the low metal doping content. From Fig. 1b, the crystal strength of B-Sm4 increases, and the relative (121) and (040) crystal planes obviously shift right. It indicates that the doping of metal Sm causes internal stress and increases the trend of the tetragonal zircon phase transition and $\text{Bi}_{1-x}\text{Sm}_x\text{VO}_4$ ($x = 0-1$) appeared [25]. In addition, the radius of the Sm^{3+} ion is 1.08 Å, which is much smaller than that of Bi^{3+} (1.17 Å) [14]. And the lattice parameters of BiVO_4 have shifted greatly after doping. According to the Scherrer formula, the particle sizes of BiVO_4 and B-Sm4 were 34 nm and 52 nm, respectively. It indicates that the intensity of the crystal was significantly enhanced. In addition, the SEM results also verify the XRD results. And in the Fig. S2b and f, the decahedral structure of B-Sm2 is less than that of BiVO_4 , and the nanosphere structure is still dominant in the SEM, which may be the reason for the low doping amount of metal Sm. In Fig. S2c and g, the decahedral structure shows significant aggregation. In the aggregated decahedral BiVO_4 crystal structure, the crystals are growing along the (010) crystal plane, which leads to more exposure of the (110) crystal plane [26]. When the metal Sm doping amount was 8 wt%, the crystal characteristics were significantly reduced (Fig. S1a and b). Fig. S2d and h show irregular grain ellipsoids. The spherical morphology dominated by grain aggregation was observed by high-power SEM, which proved that the grain aggregation is more obvious with more metal doping, so the crystal form characteristics were not obvious.

Since the bands of the (010) and (110) crystal planes of the BiVO_4 decahedron structure bend differently, the spatial structure separation of photogenerated electrons and holes occurs [26]. The photogenerated electrons accumulate on the (010) crystal plane, and the photogenerated holes accumulate on the (110) crystal plane [26]. Therefore, the exposure of the (110) crystal plane contributes to the accumulation of photogenerated holes and the oxidation ability of the photoanode, and a doping amount of 4% contributes to the photocatalytic performance of the catalyst. The main crystal planes ((104) and (110)) of $\alpha\text{-Fe}_2\text{O}_3$ are shown in Fig. 1c, Fig. S1c and d (JADE No. 33-0664), indicating that the $\alpha\text{-Fe}_2\text{O}_3$ catalyst was successfully prepared. The characteristic peaks of $\alpha\text{-Fe}_2\text{O}_3$ exist and obviously shift to the right on the B-Sm-F photoanode (Fig. S1d), which proves that $\alpha\text{-Fe}_2\text{O}_3$ combines with B-Sm4 to form B-Sm-F photoanode and binds effectively. The peak shift of the (104) and (110) crystal planes of $\alpha\text{-Fe}_2\text{O}_3$ in the B-Sm-F XRD pattern imply the coexistence of $\alpha\text{-Fe}_2\text{O}_3$ and B-Sm4 in B-Sm-F photoanode.

In Figs. S3a and 1d, the morphology of pure BiVO_4 is mainly nanospheres, and the edge tends to evolve into tetragonal zircon [27]. After Sm doping, the crystal decahedral morphology of B-Sm4 becomes increasingly obvious (Figs. S3b and 1f). The enhancement of clusters between the crystals leads to the formation of a flower-like nanocrystalline structure, which explains the enhanced crystal strength in the XRD of B-Sm4 (Fig. 1b). Figs. S3c and 1e show that pure $\alpha\text{-Fe}_2\text{O}_3$ is irregularly spherical and that the crystal structure is not obvious. According to the SEM (Figs. S3d and 1g) structure of B-Sm-F, the whole structure is mainly spherical, and the crystal structure is not obvious. In Fig. 1g, the catalyst structures of B-Sm4 and $\alpha\text{-Fe}_2\text{O}_3$ are shown. It is speculated that B-Sm-F is mainly composed of $\alpha\text{-Fe}_2\text{O}_3$ wrapped on the surface of the aggregated B-Sm4 crystal structure to form a relatively round spherical structure, so the crystallization characteristics of B-Sm-F are weakened, which is consistent with the XRD results (Fig. 1a).

As shown in Fig. S4a, the peaks of Bi 4f, V 2p, O 1s, Sm 3d and Fe 2p

can be observed in the XPS spectrum of the B-Sm-F catalyst, which proves the successful preparation of the material. According to the C 1s position in Fig. S4b, the XPS spectrum was calibrated to 284.6 eV relative to the standard carbon peak. In the Bi 4f diagram (Fig. 1h), the peaks of the three catalysts belong to Bi 4f_{7/2} and Bi 4f_{5/2}, indicating that Bi^{3+} exists in the crystal structure [28]. As shown in Fig. S4c, V 2p_{3/2} and V 2p_{1/2} are located at 516.6 eV and 524.1 eV, respectively, proving that V is a positive 5-valent ion [29]. When the metal Sm is doped in BiVO_4 , the binding energy of V 2p does not change significantly, indicating that the metal Sm doping does not affect the valence state change of V. When $\alpha\text{-Fe}_2\text{O}_3$ appears, the binding energy of V increases, which proves the electron loss around V. The XPS spectra of O 1s are shown in Fig. S4d. BiVO_4 has lattice oxygen (O_L) at 529.7 eV and an oxygen vacancy (O_V) at 531.7 eV [30], [31]. The ESR results also proved that there were oxygen vacancies on BiVO_4 , B-Sm4 and $\alpha\text{-Fe}_2\text{O}_3$ (Fig. S5). This is an inherent defect in the materials [14]. With the modification of the catalyst, the incorporation of metal Sm slightly decreased the O_L , indicating that metal Sm interacted with O. The oxygen vacancy of B-Sm4 became 530.8 eV and that of B-Sm-F became 531.1 eV. The decrease in the O_V binding energy indicates that the electrons around the O_V are enriched. This may be due to the electron transfer around Bi, resulting in the loosening and fracture of the chemical bond between Bi and O and the subsequent generation of oxygen vacancies. As shown in Fig. 1i, B-Sm4 corresponds to Sm 3d_{5/2} and Sm 3d_{3/2} at 1084.2 eV and 1111.2 eV, respectively, indicating that Sm exists at +3 valence [32]. The satellite peak due to energy loss appears at 1093.7 eV, which is also related to the oxidation state of Sm^{3+} . However, the binding energy Bi of B-Sm4 decreases, indicating that electrons are enriched around Bi, which weakens its interaction with O, and there is an interaction between Sm and O, which also proves that Sm^{3+} may replace Bi^{3+} .

The presence of Fe 2p in Fig. 1j also indicated that the B-Sm-F catalyst material was successfully prepared. The positions of 711.1 eV and 724.8 eV correspond to Fe 2p_{3/2} and Fe 2p_{1/2}, respectively, which proves the existence of Fe^{3+} in the B-Sm-F photoanode [33]. In pure $\alpha\text{-Fe}_2\text{O}_3$, 711.3 eV and 724.9 eV correspond to Fe 2p_{3/2} and Fe 2p_{1/2}, respectively. Compared with pure $\alpha\text{-Fe}_2\text{O}_3$, the binding energy of B-Sm-F photoanode decreases, indicating that electrons around Fe are enriched and that the electron transfer from B-Sm4 to $\alpha\text{-Fe}_2\text{O}_3$.

The microstructures and composition distributions of different photoanodes were further studied by TEM and EDX spectra. The B-Sm4 decahedral (110) crystal plane with a lattice spacing of 0.379 nm can be clearly observed by high-resolution TEM scanning of the B-Sm4 catalyst (Fig. S6b). EDS scanning showed that Sm was uniformly doped in BiVO_4 (Fig. S6c). In addition, the TEM pattern of the B-Sm-F catalyst (Fig. 2b) showed that the (110) main crystal plane of $\alpha\text{-Fe}_2\text{O}_3$ with a lattice spacing of 0.231 nm intersected with the (121) main crystal plane of B-Sm4. As shown in Fig. 2c, all elements are uniformly distributed on the catalyst, which also indicates the successful preparation of the B-Sm-F catalyst.

The specific surface area is an important factor affecting photocatalytic activity. Nitrogen adsorption analysis is a common method to measure the specific surface area and porous structure. Fig. S7 shows the BET characterization of the photoelectric anode catalysts. According to the Brunauer-Demin-Demin-Teller (BDDT) classification, the isotherms of the two samples are type IV, and there are H2 hysteresis loops and mesopores between 0.5 and 1.0 [34]. The pore sizes of all materials are distributed in the mesoporous region of 2–50 nm.

The specific surface area of BiVO_4 is only 2.04 m²/g. After doping with metal, the specific surface area did not increase significantly. This may be because the 4% Sm doping amount is too small, resulting in no significant increase in the specific surface area. It may be that Sm is doped into the BiVO_4 lattice with +3 valence ions, so its specific surface area is not significantly increased, which is consistent with the above XRD and SEM results. Upon further binding with $\alpha\text{-Fe}_2\text{O}_3$, the specific surface area increased significantly. The above XRD results show that the cell parameters of iron oxide are small. Therefore, although the

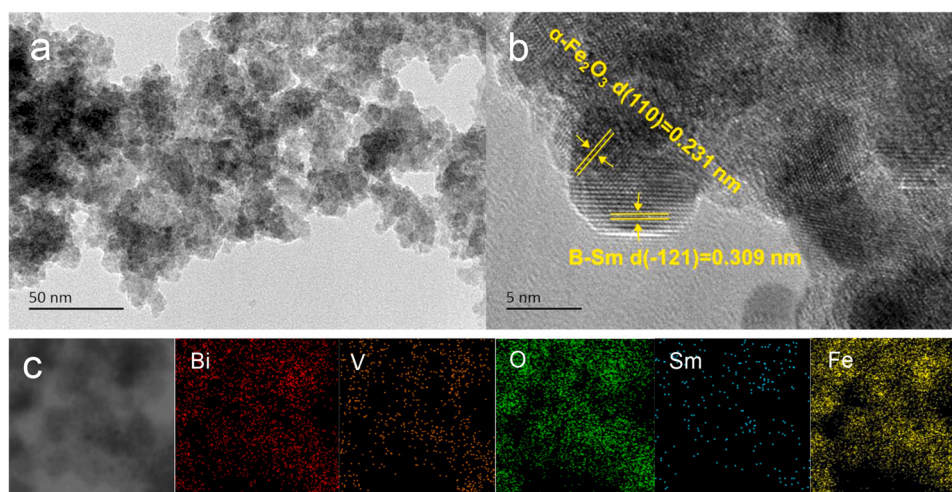


Fig. 2. (a) TEM image, (b) HR-TEM image and (c) EDS mapping of B-Sm-F.

surface pore size of the material has not changed much, the pore volume and specific surface area will increase significantly. In terms of morphology and structure, the metal Sm^{3+} replaces Bi^{3+} , forms a B-Sm4 catalyst, and then combines with $\alpha\text{-Fe}_2\text{O}_3$. Moreover, the occurrence of charge transfer between B-Sm4 and $\alpha\text{-Fe}_2\text{O}_3$ proves that there is an interaction between them.

3.2. Photoanode for BPA degradation performance

Under simulated sunlight irradiation, a three-electrode system was constructed to prepare BiVO_4 , $\alpha\text{-Fe}_2\text{O}_3$, B-Sm4 and B-Sm-F catalysts for use as working electrodes. The pollutant removal rate was measured by high-performance liquid chromatography, as shown in Fig. 3a. The degradation rate of BPA by BiVO_4 is 50.1%, the degradation rate of $\alpha\text{-Fe}_2\text{O}_3$ is 75.6%, and the degradation rate of BPA by B-Sm4 is 86.8%. This may be because Sm^{3+} as a hole trap can delay the recombination of electrons and holes [35]. At the same time, metal Sm can also speed up the charge transfer and enhance the degradation effect by increasing the number of holes. The degradation rate of BPA by B-Sm-F reached 97.5%. This shows that the heterojunction formed after recombination is conducive to reducing the recombination of photogenerated electrons and holes, thus increasing the number of active groups in the reaction process, and improving the removal rate. To verify the oxidative degradation of metal Sm in heterojunctions, BVO and $\alpha\text{-Fe}_2\text{O}_3$ were compounded together to form BVO-Fe photoanodes. The degradation rate of BVO-Fe was 88.6%, which was worse than that of B-Sm-F, validating that metal Sm plays a role in retarding the electron-hole separation in heterojunctions. After normalization, the k_{app} of the B-Sm-F photoanode is the highest (Fig. 3b), which proves that its degradation rate is the highest. Then, the condition is optimized.

The degradation tests were performed in photocatalysis, electrocatalysis and photoelectrocatalysis systems (Fig. 3c). The results show that under different systems, the degradation rates of the B-Sm-F photoanode are 36.8%, 89.1% and 97.5%, which proves that the light and electricity in the photoelectric system are synergistic. On this basis, the voltage was optimized (Fig. 3d). It was found that the greater the voltage was, the better the degradation effect. Under 2 V, the degradation rate reached 97.5%. After adjusting the pH (Fig. 3e), it was found that the degradation effect under alkaline conditions was better than that under acidic conditions and neutral conditions, and it was completely degraded within 60 min. More OH^- existed under alkaline conditions, which produced more $\cdot\text{OH}$ and enhanced the degradation of BPA by the photoanode. In conclusion, the optimized degradation conditions are as follows: PEC, 2 V, and $\text{pH}=11$. The results are also better than those in other literature (Table S2). The repeated degradation performance of B-

Sm-F is also excellent, and the degradation rate can reach 92% after five cycles (Fig. 3f).

After the catalytic degradation experiments, the results of XRD and Raman of B-Sm-F photoanode (Fig. S16) are tested to demonstrate the chemical stability of its heterojunction. In Fig. S16a, before and after degradation, the XRD characteristic peaks of the B-Sm-F photoanodes did not disappear or no new characteristic peaks appeared, which proved that the oxidative degradation process did not destroy the structure of the B-Sm-F catalyst. After enlarging it to $30^\circ\text{--}40^\circ$ (Fig. S16b), the characteristic peaks' intensity and position of $\alpha\text{-Fe}_2\text{O}_3$ (104) and (110) crystalline planes did not change either, which proves that the oxidative degradation process did not affect the intensity of Z-type heterogeneous crystalline planes of the B-Sm-F photoanode. Raman mapping (Fig. S16c) also proves that B-Sm-F structure does not change significantly before and after degradation. Peaks at 324 cm^{-1} , 359 cm^{-1} and 826 cm^{-1} represent respectively the stretching vibrations of VO_4^{3-} and V-O [53], it can be observed that there is no significant change in their intensity. The characteristic peaks of $\alpha\text{-Fe}_2\text{O}_3$ were not observed on the B-Sm-F photoanode due to the extremely low intensity of the Raman pattern of $\alpha\text{-Fe}_2\text{O}_3$ compared to that of BiVO_4 . Therefore, no change in the chemical structure of the B-Sm-F photoanode was observed after the degradation reaction, demonstrating the strong chemical stability of the synthesized B-Sm-F.

3.3. Photoelectrochemical characterization of different photoanodes

3.3.1. Research on the upconversion performance of metal Sm

To explore the photoelectrocatalytic performance of the photoanode, UV–Vis DRS spectroscopy was performed. The absorption degrees of different light anodes in the visible light region are different (Fig. 4a). The absorption range of BiVO_4 is 200–547 nm and that of B-Sm4 is 200–528 nm. The absorption range of BVO-Fe is 200–580 nm. The absorption range of $\alpha\text{-Fe}_2\text{O}_3$ is 200–678 nm and that of B-Sm-F is 200–582 nm [18,54]. The modification is conducive to improving the light absorption capacity of BiVO_4 . After Sm metal doping, the light absorption range decreases slightly, but the absorption intensity increases significantly. Compared with B-Sm2 and B-Sm8, B-Sm4 has a higher light absorption intensity (Fig. S8a) and a lower electron-hole recombination rate (Fig. S8b). This further proves that 4% Sm doping is the most beneficial for improving the photoelectrocatalytic performance of BiVO_4 . The UCPL spectrum in Fig. 4b shows that a blue purple band light is released at 447 nm and 492 nm under the excitation of 980 nm infrared light, which corresponds to a transition decline of the $^4\text{G}_{5/2}\text{--}^6\text{H}_{5/2}$ and $^4\text{G}_{5/2}\text{--}^6\text{H}_{7/2}$ energy levels, respectively [36], which explains the increase in the light absorption intensity of B-Sm4 in Fig. 4a.

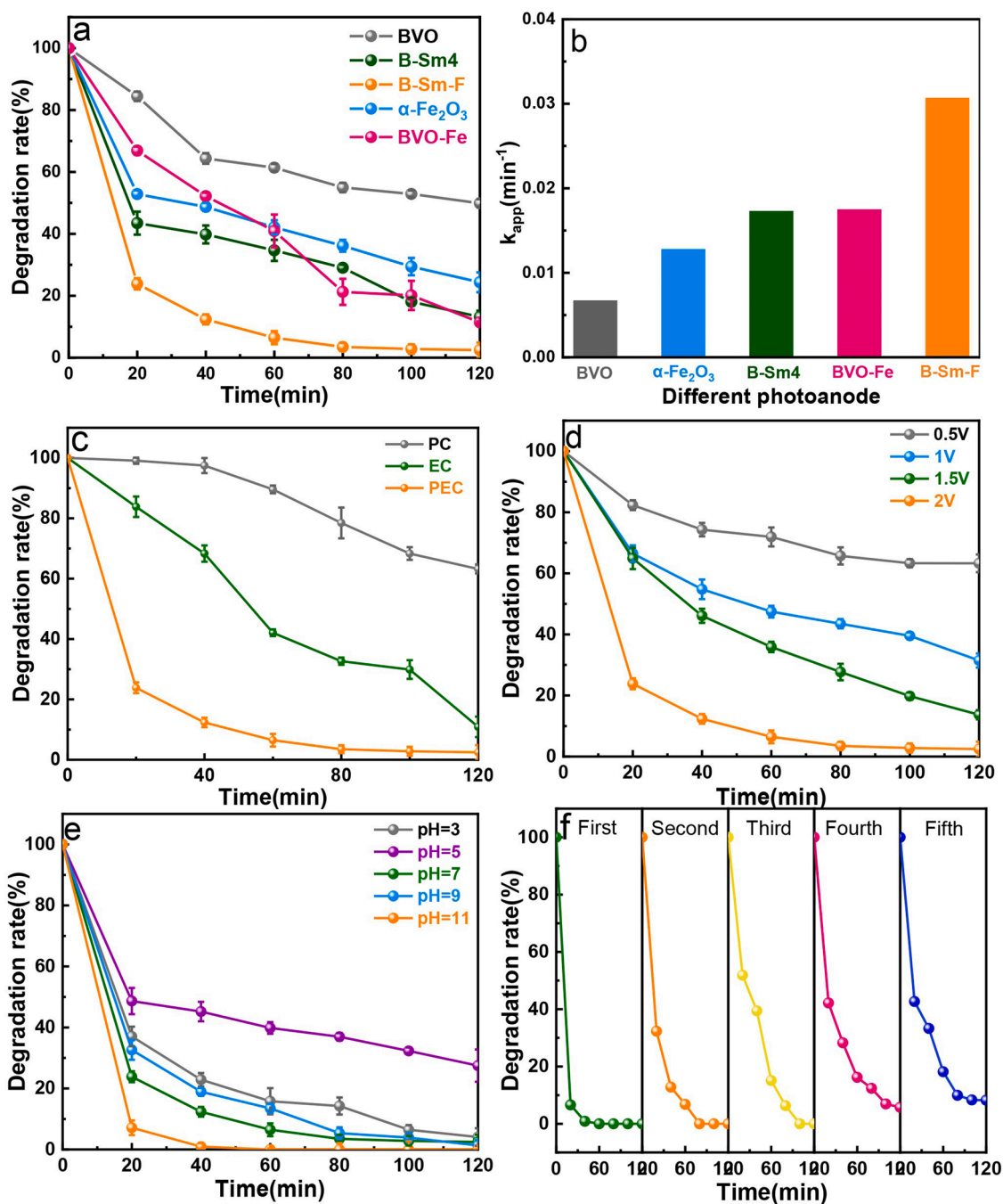


Fig. 3. (a) Effect of the photoanode on BPA degradation, (b) photoanode degradation rate constants, (c) degradation rate under different systems, (d) degradation rate under different voltages, (e) degradation rate under different pH values, and (f) stability test of the B-Sm-F photoanode (solution conditions: 20 mg of BPA in a 0.1 mol/L Na_2SO_4 electrolyte).

The above results confirm that Sm^{3+} can transform infrared light into visible light to enhance the absorption intensity of visible light by the catalyst.

In addition, the absorption range and intensity of the B-Sm-F photoanode are enhanced, which may be due to the formation of heterojunctions modified by B-Sm4 and $\alpha\text{-Fe}_2\text{O}_3$, which further causes a spectral redshift and expands the optical absorption range of the photoanode. In addition, although the absorption range of $\alpha\text{-Fe}_2\text{O}_3$ is stronger, its absorption intensity is the lowest. Combining $\alpha\text{-Fe}_2\text{O}_3$ with BiVO_4 alone to form a BVO-Fe photoanode, the light absorption range of BiVO_4 is improved in the absence of metal Sm, but its absorption intensity is greatly reduced, which further indicates the irreplaceable role of metal Sm. Therefore, B-Sm-F has the best light absorption

performance. The PL spectrum (Fig. 4c) also shows that the electron and hole recombination of B-Sm-F is the lowest, which proves that B-Sm4 and heterojunctions are successfully constructed between $\alpha\text{-Fe}_2\text{O}_3$. This further proved the UV–Vis DRS spectrum results. The band gaps of different photoelectric anodes were calculated using the UV–Vis spectra results (Fig. 4d). The band gap of B-Sm-F photoanode (2.34 eV) is reduced compared with that of B-Sm4 (2.40 eV). The narrower band gap is favorable for the jumping of photogenerated electrons, indicating that B-Sm-F is more susceptible to light excitation and electron-hole separation. From the conduction band positions of BiVO_4 , B-Sm4, B-Sm-F, and $\alpha\text{-Fe}_2\text{O}_3$ (Fig. 4e and f), it can be observed that the doping of metal Sm ($E_{\text{C-B-Sm4}} = -0.46 \text{ eV}$ vs Ag/AgCl) causes the conduction band position of BiVO_4 ($E_{\text{C-BVO}} = -0.40 \text{ eV}$ vs Ag/AgCl) to move up. It

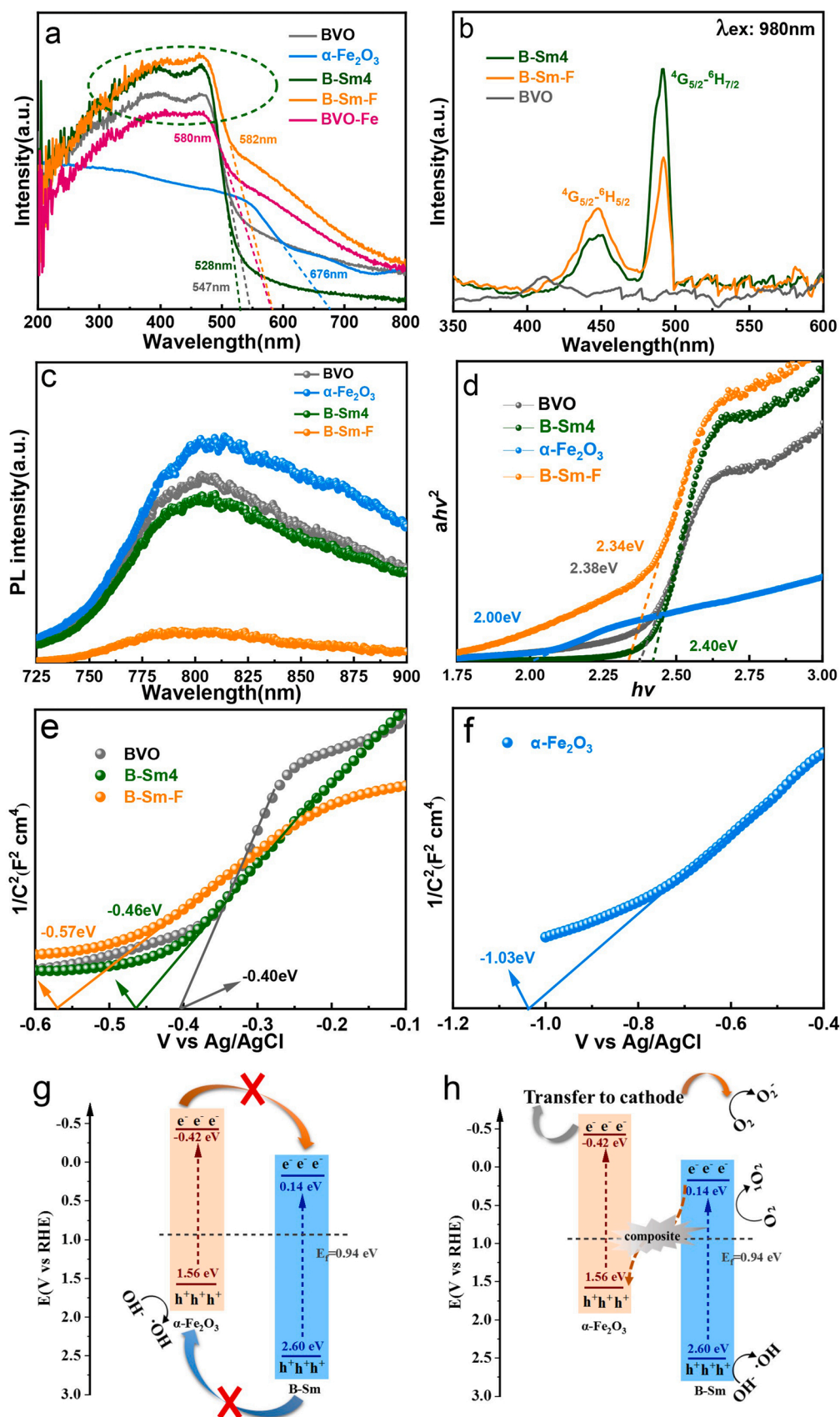


Fig. 4. (a) DRS spectra of different photoanodes, (b) UCPL spectra, (c) PL spectra, (d) Tauc plot of BiVO_4 , $\alpha\text{-Fe}_2\text{O}_3$, B-Sm4 and B-Sm-F, (e) Mott-Schottky of BiVO_4 , B-Sm4 and B-Sm-F, and (f) Mott-Schottky of $\alpha\text{-Fe}_2\text{O}_3$, the schematic of B-Sm-F charge transfer mechanism (g) Type II heterojunction and (h) Z-type heterojunction.

indicates that its conduction band position can accumulate more charges, which is conducive to the separation of electrons and holes. The formation of B-Sm-F photoanodes with more negative conduction band positions ($E_{C-B-Sm-F} = -0.57$ eV vs Ag/AgCl) indicates the interaction between $\alpha\text{-Fe}_2\text{O}_3$ and B-Sm4, resulting in easier separation of its electrons and holes. Combining the valence and conduction band positions of B-Sm4 and $\alpha\text{-Fe}_2\text{O}_3$, Z-type heterojunction scheme is proposed and others such as type II are excluded. In the Z-type heterojunction scheme, electrons will transfer from B-Sm4 to $\alpha\text{-Fe}_2\text{O}_3$ through the heterojunction interface, creating a built-in electric field at the interface. If the electron transfer direction is from $\alpha\text{-Fe}_2\text{O}_3$ to B-Sm4, it is not consistent with the XPS results. And the VB potential of $\alpha\text{-Fe}_2\text{O}_3$ (1.56 eV) was lower than the oxidation potential of the $\text{H}_2\text{O}/\cdot\text{OH}$ redox pair (2.27 eV), which contradicts the results of the ESR experiment (Fig. S12c). However, in the Z-type heterojunction scheme, B-Sm4 has a VB potential of 2.60 eV and can generate $\cdot\text{OH}$ by oxidizing H_2O , which is in accordance with the results in Fig. S12c. On the other hand, the CB potential of $\alpha\text{-Fe}_2\text{O}_3$ is -0.42 eV, which is lower than the reduction potential of the $\text{O}_2/\text{O}_2^{\cdot-}$, capable of generating $\cdot\text{O}_2^{\cdot-}$, which is in accordance with the results of Fig. S12d. As a result, the heterojunction type of the photoanode catalyst material is a Z-type heterojunction (Fig. 4g and h).

Based on the forbidden band width (E_B) (Fig. 4d) and the conduction band position (E_C) (Fig. 4e) of different photoanodes, the valence band position (E_V) can be calculated with the Eq. (5) [18].

$$E_V = E_C + E_B \quad (5)$$

The conduction band position at the RHE potential can be calculated according to Eq. (S9). The top of the valence band is calculated to be 2.54 eV for B-Sm4 and 1.54 eV for $\alpha\text{-Fe}_2\text{O}_3$. To further obtain the

valence band position of the photoanode accurately, the UPS test was performed on the photoanode (Fig. S18). The results show that the valence band position of B-Sm is 2.60 eV and that of $\alpha\text{-Fe}_2\text{O}_3$ is 1.56 eV, which is consistent with the results obtained from the above calculations. And it fully proves that the charge transfer between B-Sm4 and $\alpha\text{-Fe}_2\text{O}_3$ is in the form of a Z-type heterojunction. In summary, the main effect of doping with metal Sm is to improve the absorption intensity of the photoanode for visible light, and the separation of electrons and holes mainly depends on the effect of the heterojunction.

3.3.2. Effect of metal Sm on the charge transfer of heterojunctions

To further clarify the electrochemical performance of the prepared B-Sm-F photoanode, the LSV of the photoanode was tested. As shown in Fig. 5a, the LSV values of different photoanodes were measured in 1 mol/L NaOH (pH=13) and 1 mol/L Na_2SO_3 (pH=13) solutions under light. Fig. 5b shows the bias photon current conversion efficiency (Eq. (S1)). At the same time, the light capture efficiencies (LHE, Eq. (S2)) of different photoanodes (Fig. S9a) were calculated from the AM 1.5 G sunlight spectrum (Fig. S9b) to obtain the charge injection efficiency (Fig. 5c) (Eq. (S3)) and charge separation efficiency (Fig. 5d) (Eq. (S4)). The current density of B-Sm-F is the highest. In addition, in Fig. 6b, the bias photon current conversion efficiencies of BiVO_4 , B-Sm4, $\alpha\text{-Fe}_2\text{O}_3$ and B-Sm-F are 0.02%, 0.12%, 0.26% and 1.11%, respectively, which indirectly proves that the construction of the heterojunction significantly inhibits the recombination of electrons and holes. The charge injection efficiencies of BiVO_4 , B-Sm4, $\alpha\text{-Fe}_2\text{O}_3$ and B-Sm-F are 1.7%, 11.6%, 8.4% and 26.0%, respectively (at 1.23 V vs RHE), and the charge separation efficiency values are 1.2%, 40.0%, 30.9% and 48.8%, respectively (at 1.23 V vs RHE). This shows that the doping of metal Sm

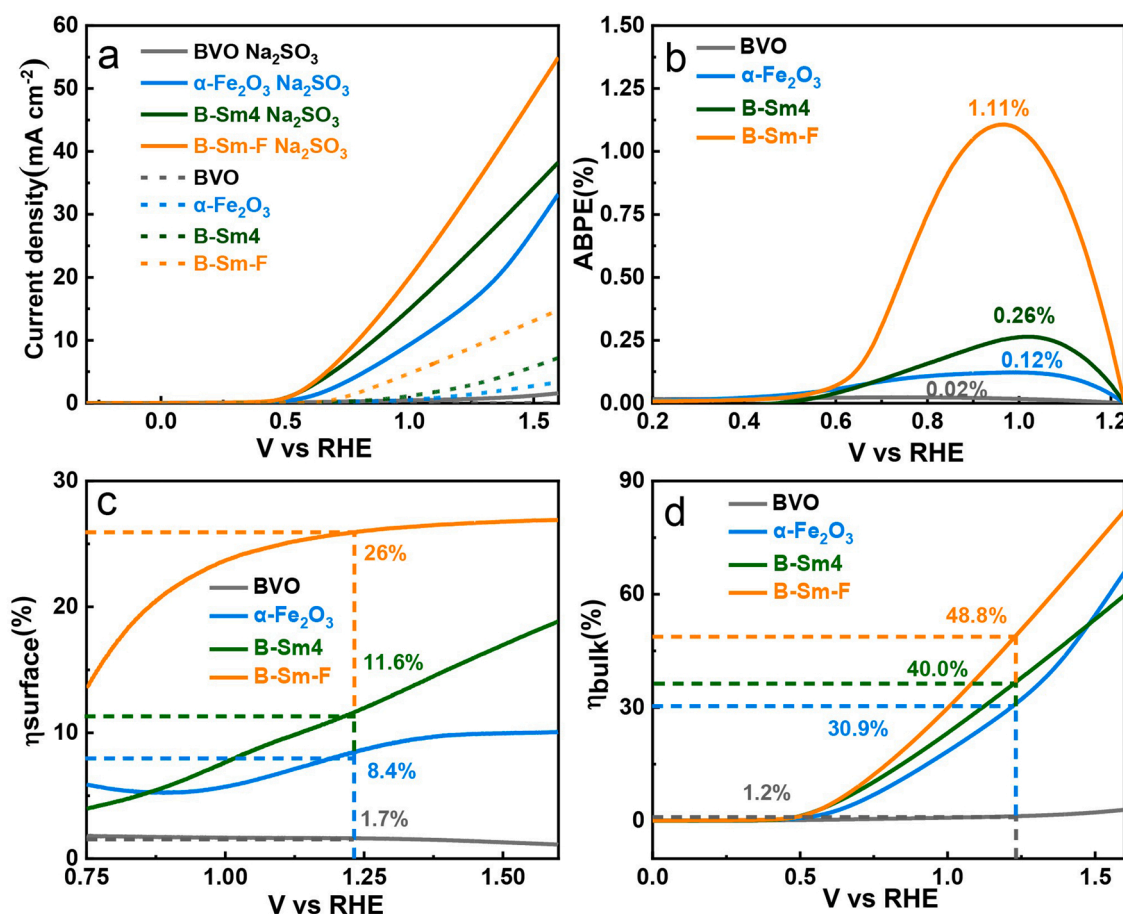


Fig. 5. (a) Linear volt ampere sweeps curve (LSV), (b) ABPE, (c) charge injection efficiency (η_{Surface}), and (d) charge separation efficiency (η_{bulk}) of different photoanodes.

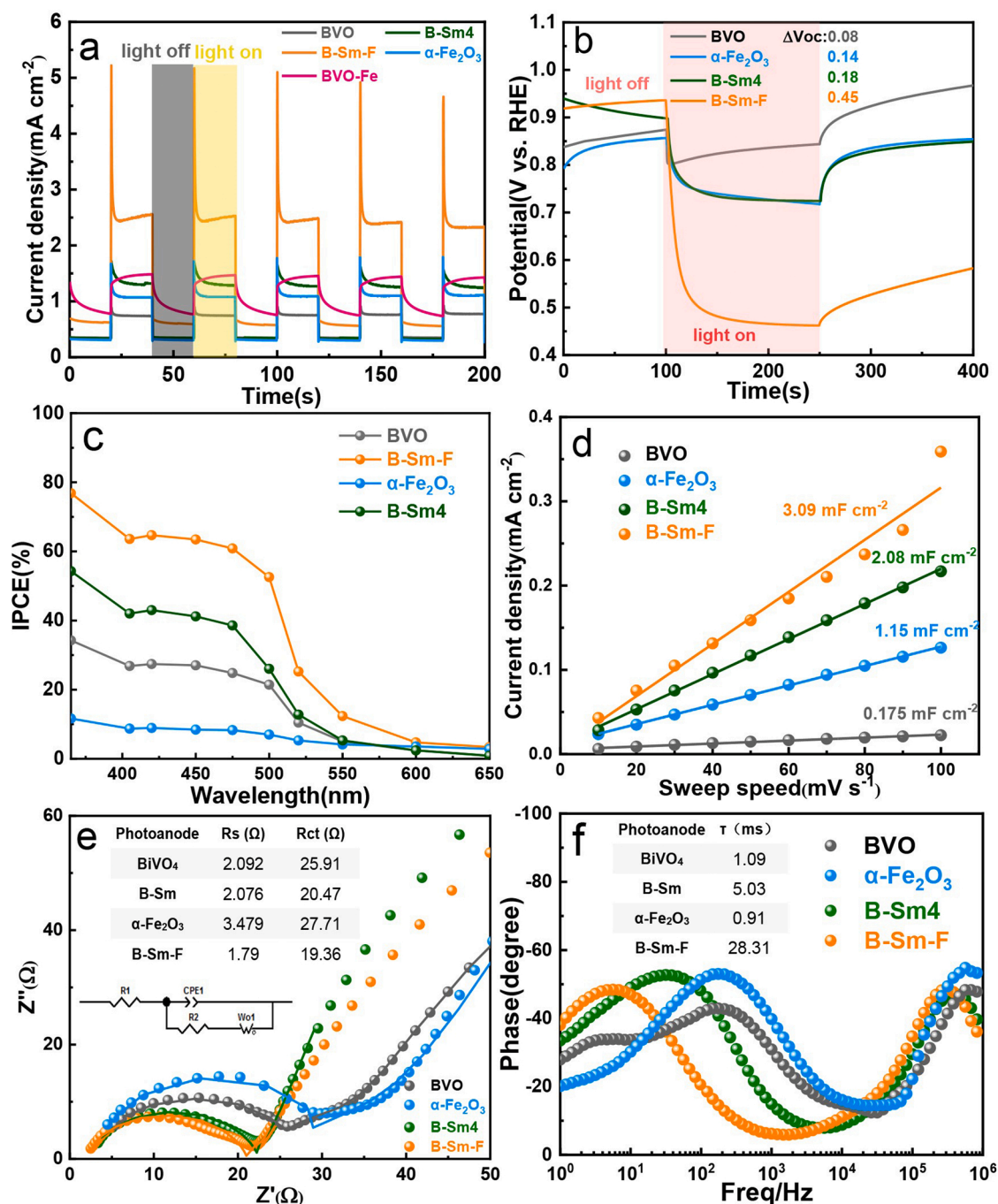


Fig. 6. (a) I-T (1.23 V vs RHE), (b) OCPT, (c) IPCE, (d) ECSA, (e) EIS spectra under illumination, and (f) a Bode diagram of different photoanodes.

is conducive to charge transfer between the two semiconductors. It can significantly improve the charge injection efficiency of BiVO₄, which greatly improves the water oxidation ability of BiVO₄. However, metal Sm cannot directly increase the optical current density of BiVO₄ by doping, which requires consideration of the effect of the inherent oxygen vacancies in the material [14]. For this study, Sm doping increases the doping amount of O_V as an electron donor doping agent. An appropriate doping amount can increase the carrier concentration of BiVO₄ and improve the conductivity [37]. α -Fe₂O₃ can help B-Sm4 significantly improve its charge separation efficiency and greatly inhibit the recombination of electrons and holes, indicating that to keep their original electron affinity potential and work function unchanged, a space charge region is formed between the two semiconductors so that the heterojunction can function stably.

To further explore the photoelectric performance of different photoanodes, Fig. 6a shows the I-T of different photoanodes under alternating light and dark conditions at 1.23 V vs RHE. Fig. 6b shows the open circuit voltage (OCP) test. Fig. 6c shows the IPCE (Eq. (S5)). The electrochemical active area (ECSA) (Fig. 6d) was calculated according to Fig. S10.

The intermittent duration of photoanode stability recording is 20 s, and the photoelectric density of unmodified BiVO₄ can reach 0.74 mA/cm² (Fig. 6a). With continuous modification, the current density also increases. Finally, the photocurrent density of the photoelectrode reached 2.50 mA/cm². The photocurrent density of pure BVO-Fe photoanode is 1.43 mA/cm², which is lower than B-Sm-F. It is proved that the metal Sm plays a role in increasing the photocurrent in the B-Sm-F photoanode. It is proven that the modification of BiVO₄ significantly

inhibits the recombination of electrons and holes and improves its photoelectric performance. In addition, BiVO₄, α -Fe₂O₃, B-Sm4 and B-Sm-F photoanodes have spikes at a moment of turning on the lamp, which proves that these photoanodes have different degrees of photocurrent attenuation in the PEC process. However, with continuous modification, the time required for photocurrent attenuation also becomes increasingly longer, indicating that the transfer speed of interface charge in the semiconductor is also faster [21]. The larger the spike current is, the more serious the photocurrent attenuation is, which proves that there are more surface traps. This is due to the presence of more oxygen vacancies on the surface, introducing new recombination centres [38]. In addition, the OCP of the photoanode was tested (Fig. 6b). After 100 s without light, light was added, and the process was continued for 150 s. We observed a change in the open circuit voltage. It was found that under light, all photoelectrodes produced a photo-generated potential opposite to the bias voltage, resulting in a decrease in the open circuit voltage. The photovoltage of the photoanode is formed by the gradient of the quasi-Fermi level under steady-state light. It is the driving force for injecting photogenerated holes into electrolytes for the reaction [39]. When the lamp is turned on, the OCP systematically increases from the BiVO₄ to the B-Sm-F photoanode. When the voltage difference is larger, the band bending at the photoanode/electrolyte interface increases, and the electron-hole separation increases [40].

To understand the solar current conversion characteristics, the IPCE of the photoanode was tested and calculated under 1.23 V vs RHE voltage, as shown in Fig. 6c. The IPCE values of all photoanodes are basically 550 nm, which is consistent with the results in UV-Vis (Fig. 4a). α -Fe₂O₃ had the lowest photoelectric conversion rate of 11.6%. The photocurrent conversion was increased from 33.9% to 54.2% after doping with 4% of metal Sm. However, after modification, the photocurrent conversion efficiency of B-Sm-F reached 76.5% with 2.37 times increase. This is due to the conversion of infrared light into the visible light band by Sm³⁺ (Fig. 4b), which improves the light absorption capacity of pure BiVO₄ at 400–500 nm (Fig. 4a). At the same time, the photoelectric conversion efficiency at 600–650 nm is higher than that of pure BiVO₄, which is attributed to the combination of α -Fe₂O₃ enhancing the light utilization efficiency of the catalyst material at 600–650 nm [41]. The B-Sm-F photoanode also has a higher active area (Fig. 6d). The ultrathin crystal structure and abundant oxygen vacancies can effectively promote hole transport/capture and provide more active sites for water oxidation, so it has better PEC activity [42].

To further clarify the charge transfer inside the photoanode and at the photoanode/electrolyte interface, EIS was performed under visible light (Fig. 6e), and the fitted equivalent circuit diagram was attached. The equivalent circuit diagram includes the solution resistance (R_s) and charge transfer resistance (R_{ct}) of the photoanode, namely, the difficulty of charge transfer through the interface between the electrode and the electrolyte solution [43]. According to Fig. 6e, when metal Sm is doped, its R_{ct} decreases from 25.91 Ω to 20.47 Ω , which proves that metal Sm significantly reduces the electrode/electrolyte interface resistance and is conducive to charge transfer and transmission. Therefore, the charge injection efficiency of the photoanode can be improved, which is consistent with the results of Fig. 5c. The Bode diagram results show that the carrier life (Eq. S6) increases with continuous modification (Fig. 6f). The carrier lifetime of pure BiVO₄ is 1.09 ms. The carrier lifetime of α -Fe₂O₃ is 0.91 ms, while that of B-Sm-F is 28.31 ms. And to further explore the photogenerated charge carrier lifetime of the photoanodes accurately, the TRPL was measured. The TRPL (Fig. S17) and its calculation results (Table S8) show that a comparison of the photoanodes' photogenerated charge carrier lifetime can be found: α -Fe₂O₃ < BVO < B-Sm4 < BVO-Fe < B-Sm-F. The carrier lifetime is greatly improved, which proves that a heterojunction is formed between semiconductors, which inhibits the recombination of electrons and holes and is conducive to charge transfer and transmission. The above results show that the performance of metal Sm cannot be directly changed by

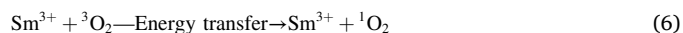
doping, but is mainly achieved by increasing the content of oxygen vacancies in BiVO₄ and reducing its charge transfer resistance to improve the photoelectric performance of BiVO₄, while charge separation mainly relies on the Z-type heterojunction.

3.4. Degradation mechanism in the oxidation system of the B-Sm-F photoanode

3.4.1. Degradation pathway and reactive oxygen species analysis

To preliminarily explore the degradation mechanism, the intermediate products of the samples were analysed by high-performance liquid chromatography–mass spectrometry (HPLC–MS) (Fig. S11). The results are as follows. It can be inferred from the intermediate products that the degradation path mainly depends on the oxidative fracture of the C-C bond and the electrophilic addition reaction of hydrogen and water (Fig. 7f). To further explore the active substances leading to degradation in the system, a free radical quenching experiment and ESR test was conducted for the degradation process [6,44].

In the quenching experiment, FFA quenching of ¹O₂ inhibited the degradation efficiency by 36%, TBA quenching of \cdot OH inhibited the degradation efficiency by 44%, EDTA-2Na quenching of h⁺ inhibited the degradation efficiency by 20%, and BQ quenching of \cdot O₂⁻ inhibited the degradation efficiency by 43% (Fig. S12a). Therefore, the dominant free radicals in the degradation process are ¹O₂, \cdot OH and \cdot O₂⁻. The ESR test also proved that there ¹O₂, \cdot OH and \cdot O₂⁻ exist (Fig. S12). These active substances are strongly oxidative and can attack the C-C bond to degrade BPA (degradation path 1) (Fig. 7f) [44]. From the generation mechanism of ¹O₂, there are oxygen vacancies on the catalyst surface (oxygen vacancies also need to be tested), which is conducive to the physical adsorption of molecular O₂ [45]. Oxygen molecules will not directly generate singlet oxygen under light. It is necessary for sensitizers to be excited by light radiation and then transfer energy to O₂ to generate ¹O₂ [46]. Sm³⁺ is a good photosensitizer [47], so singlet oxygen is generated. The process is shown in Equation (6). After the simultaneous addition of metal Sm, the degradation rate of the B-Sm4 photoanode was increased by 36% compared with that of the BiVO₄ photoanode (Fig. 3a), which was consistent with the quenching experimental data (Fig. S12a) and proved that the single linear state oxygen production was correlated with metal Sm.



Oxygen in water produces not only singlet oxygen but also \cdot O₂⁻. However, when O₂ is converted to \cdot O₂⁻, the conduction band potential of the catalyst should reach - 0.33 eV, and the catalyst on the photoanode should meet the O₂ generation \cdot O₂⁻, which can enhance the oxidation ability of the photoanode [48].

3.4.2. Degradation mechanism by theoretical calculations

The above degradation pathway has not been effectively verified. Therefore, this paper uses DFT calculations to calculate the front-line orbitals (Table S3), the electrostatic potential (ESP) and the Fukui function of BPA (Fig. 7), and Fukui function analysis is performed (Fig. 7c-e, Table S4) to predict and analyse the above reaction sites. The LUMO orbital refers to the lowest unoccupied molecular orbital of the molecule, which is related to the nucleophilic reaction. HOMO refers to the highest occupied molecular orbital of the molecule, which is related to the electrophilic reaction. According to the composition of the two, the difficulty of achieving electrophilic and nucleophilic reactions can be judged. At the same time, the energy difference between the two is called the "energy band gap", which can effectively judge whether the molecule is easily excited. From the LUMO and HOMO orbitals of BPA molecules, the oxidation potential of BPA is - 0.04 eV (Table S3), while the oxidation potential of the photoanode is 2.54 eV. Therefore, photoanodes can effectively degrade BPA.

To describe the relationship between adsorption behaviour and

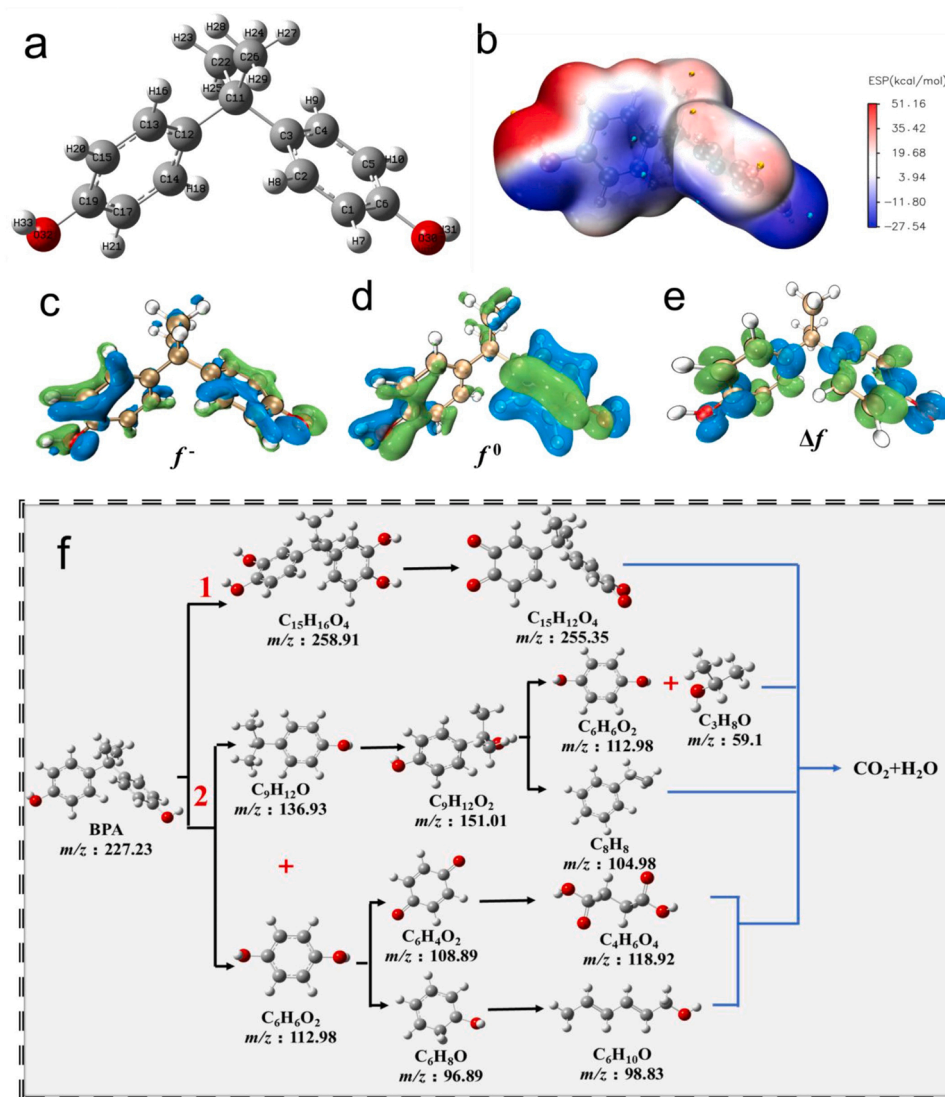


Fig. 7. (a) BPA chemical structure, (b) ESP, (c) f^- , (d) f^0 , (e) Δf , and (f) the degradation path of BPA under the B-Sm-F photoanode.

electron density, the surface ESP of the BPA molecule was analysed (Fig. 7b). When the electrostatic potential is higher, the surface electron density distribution is more uneven, and when the surface electrostatic potential is positive, it can attract negative charges, and the greater the value is, the stronger the adsorption capacity. When the surface electrostatic potential is negative, it can attract positive charges. The positive electrostatic potential is distributed around the adjacent carbon of hydroxyl carbon and hydroxyl carbon, indicating that it has a strong adsorption capacity for negatively charged radicals such as $\cdot\text{OH}$ and $\cdot\text{O}_2$. However, ESP cannot accurately locate the adsorption attack site of free radicals, so Fukui function analysis was performed on BPA.

In the results of Table S4, the charge distribution of the neutral state (q_N), cationic state (q_{N-1}) and anionic state (q_{N+1}) of the BPA molecule are calculated by the Hirshfeld model to obtain the favourable sites for electrophilic attack (f^-), nucleophilic attack (f^+), free radical attack (f^0) and double descriptors of the molecule (Δf) and visualize it (Fig. 7c, d and e). $\cdot\text{OH}$ belongs to a group with few electrons, which more easily attacks the favourable sites of electrophilic attack of BPA (where the density of the electron cloud is high). Except for the O30, O32, C6 and C19 sites with high density electron clouds caused by the hydroxyl group, C3, C12, C5 and C15 all show high f^- values, which proves that the densities of the electron clouds at the four sites are high, and they are very vulnerable to electrophilic attack. Therefore, degradation path 1

and degradation path 2, as shown in Fig. 7f, appear. From the f^0 value, the C15 and C5 sites have the highest values after removing the O32 and O30 sites, which proves that they are affinity sites attacked by free radicals, which conforms to the results of degradation pathway 1 (Fig. 7f).

In addition, Δf can show both nucleophilic and electrophilic reaction sites at the same time, so f^- and f^+ do not need to be considered. The smaller its value is, the greater the possibility of electrophilic attack on the reaction site is. The larger its value is, the greater the possibility of nucleophilic attack on the reaction site is. C3 and C12 are also favourable sites for the electrophilic attack, further indicating that pathway 2 is the preferred degradation pathway (Fig. 7f).

Organic compounds with structures similar to BPA are called bisphenol analogues. In this study, front-line orbit calculations and Fukui function calculations were performed for the BPC, BPE and BPF. The calculation results of front-line orbitals for BPA, BPC, BPE and BPF are shown in Table S3. Organic compounds with high HOMO potential and low band gap energy are more easily degraded by ROS attack [49]. There is no significant difference in the band gap energy values of the four molecules, indicating that the slight difference in molecular structure does not affect the electron transfer rate and structural stability of the molecule. The reason may be that BPA, BPC, BPE and BPF have extremely spatial sizes and symmetry between similar HOMO-LUMO

orbitals. The charge density distributions of the four molecules are then further explored by ESP (Fig. 7b, Fig. S13b, Fig. S14b, Fig. S15b). The high surface electrostatic potential is mainly distributed near two hydroxyl groups, which is determined by the similar structure of bisphenol analogues. However, the order of electrostatic potential is BPA (51.16 kcal/mol) > BPF (50.66 kcal/mol) > BPE (50.50 kcal/mol) > BPC (49.74 kcal/mol). The BPA surface electrostatic potential is higher, indicating that its ability to adsorb free radicals is stronger, which is conducive to the degradation of BPA. To further determine the ROS attack site, Fukui function analysis was performed on four molecules.

Comparing the Fukui functions of the four molecules (Tables S4–S7), it can be observed from Δf that the hydroxyl oxygen atom of BPC, BPE and BPF, the carbon atom connected to the hydroxyl oxygen atom and its para-position carbon are the most vulnerable to electrophilic attack, which is consistent with the analysis results of the Fukui index of BPA molecules, indicating that electrophilic oxidants degrade bisphenol analogues into small molecules by preferentially attacking the para-carbon of the hydroxyl group. There is electrophilic selective aggression between the structures of $^1\text{O}_2$ and bisphenol analogues [45], which is because $^1\text{O}_2$ is a highly selective nonradical oxidant with unoccupied π -2p molecular orbitals and thus has strong electrophilic reactivity [50, 51]. In summary, it is proven that $^1\text{O}_2$ mainly attacks the para carbon of the hydroxyl group. In addition, the hydroxyl neighboring carbons C1, C5, C15 and C17 of the BPA molecule, the hydroxyl neighboring carbons C1, C5, C14 and C16 of the BPC molecule, the hydroxyl neighboring carbons C1, C5, C16 and C18 of the BPE molecule, and the hydroxyl neighboring carbons C1, C5, C17 and C19 of BPF molecules have higher f^0 values, which proves that the hydroxyl neighboring carbons are favourable sites for free radical attack. $\cdot\text{OH}$ and $\cdot\text{O}_2$ attack organic compounds belonging to free radical attack, which proves that reactive oxygen radicals tend to selectively attack hydroxyl neighboring carbon.

4. Conclusions

In summary, 4 wt% metal Sm was loaded on BiVO_4 and formed a B-Sm-F photoanode with $\alpha\text{-Fe}_2\text{O}_3$ to explore the role of Sm in the PEC system. It was found that the metal Sm can convert infrared light (980 nm) to blue–violet light (400–500 nm), further enhancing the absorption intensity of the photoanode to visible light. At the same time, Sm doping reduces the interface charge transfer resistance of the photoanode from 25.91 Ω to 20.47 Ω , which improves the charge injection efficiency and charge transfer efficiency of the photoanode. In the oxidation system, the metal Sm is a good photosensitizer and can increase the content of oxygen vacancies on the surface of the photoanode, which is beneficial to the metal Sm to transfer energy to O_2 adsorbed in the oxygen vacancies and convert it to $^1\text{O}_2$, which is beneficial to the degradation of bisphenol A in the system. After modification, the degradation rate of the photoanode reached 100% within 60 min. In addition, there was no significant difference in band gap energy due to the same parent structure of bisphenol compounds. The calculated results of the Fukui function show that there are two main ways to degrade bisphenol analogues. One is the nonradical $^1\text{O}_2$ attacking the para-carbon on the hydroxyl carbon, and the other is the reactive oxygen radicals $\cdot\text{OH}$ and $\cdot\text{O}_2$ attacking the neighboring-carbon on the hydroxyl carbon, indicating that the reactive oxygen radicals selectively attack phenolic compounds at different sites. This study may provide a new method for the directional mineralization of bisphenol analogues by doping metal Sm.

CRediT authorship contribution statement

Yiran Chen: Conceptualization, Methodology, Investigation, Date curation, Formal analysis, Visualization, Writing – original draft. **Lu Liu:** Date curation, Visualization. **Lu Zhang:** Date curation,

Visualization. **Shunlin Li:** Methodology, Formal analysis. **Xinyu Zhang:** Investigation. **Wenchao Yu:** Investigation. **Feng Wang:** Date curation. **Wanlai Xue:** Investigation. **Hui Wang:** Conceptualization, Supervision, Writing – review & editing, Funding acquisition, Project administration. **Zhaoyong Bian:** Conceptualization, Supervision, Writing – review & editing, Funding acquisition.

Declaration of Competing Interest

The authors declare that they have no known competing financial interests or personal relationships that could have appeared to influence the work reported in this paper.

Data availability

Data will be made available on request.

Acknowledgments

This work was supported by the National Natural Science Foundation of China (No. 52270057 and 52070015), Beijing Natural Science Foundation of China (No. 8222061), and Beijing Forestry University Outstanding Young Talent Cultivation Project (No. 2019JQ03007).

Appendix A. Supporting information

Supplementary data associated with this article can be found in the online version at doi:10.1016/j.apcatb.2023.122775.

References

- [1] Y. Li, H. Zhang, A. Rashid, A. Hu, K. Xin, H. Li, B. Adyari, Y. Wang, C.P. Yu, Q. Sun, Bisphenol A attenuation in natural microcosm: Contribution of ecological components and identification of transformation pathways through stable isotope tracing, *J. Hazard. Mater.* 385 (2020), 121584, <https://doi.org/10.1016/j.jhazmat.2019.121584>.
- [2] D. Fan, W. Yin, W. Gu, M. Liu, J. Liu, Z. Wang, L. Shi, Occurrence, spatial distribution and risk assessment of high concern endocrine-disrupting chemicals in Jiangsu Province, China, *Chemosphere* 285 (2021), 131396, <https://doi.org/10.1016/j.chemosphere.2021.131396>.
- [3] J. Gao, R.F. Nunes, K. O'Shea, G.L. Saylor, L. Bu, Y.G. Kang, X. Duan, D. Dionysiou, S. Luo, UV/Sodium percarbonate for bisphenol A treatment in water: Impact of water quality parameters on the formation of reactive radicals, *Water Res.* 219 (2022), 118457, <https://doi.org/10.1016/j.watres.2022.118457>.
- [4] C. Karrer, W. de Boer, C. Delmaar, Y. Cai, A. Crépet, K. Hungerbühler, N. von Goetz, Linking probabilistic exposure and pharmacokinetic modeling to assess the cumulative risk from the bisphenols BPA, BPS, BPF, and BPAF for Europeans, *Environ. Sci. Technol.* 53 (2019) 9181–9191, <https://doi.org/10.1021/acs.est.9b01749>.
- [5] L. Zhang, C. Wei, H.Y. Tang, H. Wang, Z.Y. Bian, Construction of heterojunction photoanode via facile synthesis of CoOx/CN nanocomposites for enhanced visible-light-driven photoelectrochemical degradation of clofibric acid, *Chemosphere* 281 (2021), 130825, <https://doi.org/10.1016/j.chemosphere.2021.130825>.
- [6] Z. Zheng, Y.H. Ng, Y. Tang, Y. Li, W. Chen, J. Wang, X. Li, L. Li, Visible-light-driven photoelectrocatalytic activation of chloride by nanoporous $\text{MoS}_2/\text{BiVO}_4$ photoanode for enhanced degradation of bisphenol A, *Chemosphere* 263 (2021), 128279, <https://doi.org/10.1016/j.chemosphere.2020.128279>.
- [7] H. Shao, Y. Wang, H. Zeng, J. Zhang, Y. Wang, M. Sillanpää, X. Zhao, Enhanced photoelectrocatalytic degradation of bisphenol A by BiVO_4 photoanode coupling with peroxymonosulfate, *J. Hazard. Mater.* 394 (2020), 121105, <https://doi.org/10.1016/j.jhazmat.2019.121105>.
- [8] Y. Zhao, Z. Han, G. Gao, W. Zhang, Y. Qu, H. Zhu, P. Zhu, G. Wang, Dual functions of CO_2 molecular activation and 4f levels as electron transport bridge in dysprosium single atom composite photocatalysts with enhanced visible-light photoactivities, *Adv. Funct. Mater.* 31 (2021), 2104976, <https://doi.org/10.1002/adfm.202104976>.
- [9] Z. Shen, H. Li, H.S. Hao, Z.G. Chen, H.M. Hou, G.L. Zhang, J.R. Bi, S. Yan, G.S. Liu, W.Y. Gao, Novel Tm^{3+} and Yb^{3+} co-doped bismuth tungstate up-conversion photocatalyst with greatly improved photocatalytic properties, *J. Photoch. Photobio. A* 380 (2019), 111864, <https://doi.org/10.1016/j.jphotochem.2019.111864>.
- [10] J. Zhou, X. Rong, P. Zhang, M.S. Molokeev, P. Wei, Q. Liu, X. Zhang, Z. Xia, Manipulation of $\text{Bi}^{3+}/\text{In}^{3+}$ transmutation and Mn^{2+} -doping effect on the structure and optical properties of double perovskite $\text{Cs}_2\text{NaBi}_{1-x}\text{In}_x\text{Cl}_6$, *Adv. Opt. Mater.* 7 (2019), 1801435, <https://doi.org/10.1002/adom.201801435>.
- [11] T. Liu, G. Tan, C. Zhao, C. Xu, Y. Su, Y. Wang, H. Ren, A. Xia, D. Shao, S. Yan, Enhanced photocatalytic mechanism of the Nd-Er co-doped tetragonal BiVO_4

- photocatalysts, *Appl. Catal. B. Environ.* 213 (2017) 87–96, <https://doi.org/10.1016/j.apcatb.2017.05.018>.
- [12] S. Moscow, V. Kavinkumar, M. Sriramkumar, K. Jothivenkatachalam, P. Saravanan, N. Rajamohan, Y. Vasseghian, M. Rajasimman, Impact of Erbium (Er) and Yttrium (Y) doping on BiVO₄ crystal structure towards the enhancement of photoelectrochemical water splitting and photocatalytic performance, *Chemosphere* 299 (2022), 134343, <https://doi.org/10.1016/j.chemosphere.2022.134343>.
- [13] R. Chen, W. Wang, D. Jiang, X. Chu, X. Ma, Q. Zhan, Hydrothermal synthesis of Nd³⁺ doped heterojunction ms/tz-BiVO₄ and its enhanced photocatalytic performance, *J. Phys. Chem. Solids* 117 (2018) 28–35, <https://doi.org/10.1016/j.jpcs.2018.02.010>.
- [14] G.V. Govindaraju, J.M. Morbec, G.A. Galli, K.S. Choi, Experimental and computational investigation of lanthanide ion doping on BiVO₄ photoanodes for solar water splitting, *J. Phys. Chem. C* 122 (2018) 19416–19424, <https://doi.org/10.1021/acs.jpcc.8b05503>.
- [15] K. Yan, J. Liu, J. Qin, J. Zhang, A portable solar light-driven biophotocatalytic system for pollutant removal powered by photovoltaic cells, *J. Hazard. Mater.* 435 (2022), 128989, <https://doi.org/10.1016/j.jhazmat.2022.128989>.
- [16] N. Liu, D. Ouyang, Y. Cai, Y. Li, Heterostructured Fe₂O₃/BiVO₄ nano-photocatalyst for the reduction of nitroarenes into amines, *Ceram. Int.* 46 (2020) 24534–24543, <https://doi.org/10.1016/j.ceramint.2020.06.240>.
- [17] Q.Z. Wang, J.J. He, Y.B. Shi, S.L. Zhang, T.J. Niu, H.D. She, Y.P. Bi, Z.Q. Lei, Synthesis of MFe₂O₄ (M=Ni, Co)/BiVO₄ film for photoelectrochemical hydrogen production activity, *Appl. Catal. B. Environ.* 214 (2017) 158–167, <https://doi.org/10.1016/j.apcatb.2017.05.044>.
- [18] L. Zhang, X.Y. Zhang, C. Wei, F. Wang, H. Wang, Z.Y. Bian, Interface engineering of Z-scheme α-Fe₂O₃/g-C₃N₄ photoanode: Simultaneous enhancement of charge separation and hole transportation for photoelectrocatalytic organic pollutant degradation, *Chem. Eng. J.* 435 (2022), 134873, <https://doi.org/10.1016/j.cej.2022.134873>.
- [19] S. Rana, K.K. Yadav, K.S. Ankush, S.K. Mehta, M. Jha, Low temperature hydrothermal method for synthesis of crystalline Fe₂O₃ and their oxygen evolution performance, *Electroanalysis* 32 (2020) 2528–2534, <https://doi.org/10.1002/elan.202060146>.
- [20] Y.J. Yan, Y.Y. Peng, Y.C. Song, R.Y. Wang, H. Wang, Z.Y. Bian, Polyethyleneimine-reinforced Sn/Cu foam dendritic self-supporting catalytic cathode for CO₂ reduction to HCOOH, *Chemosphere* 301 (2022), 134704, <https://doi.org/10.1016/j.chemosphere.2022.134704>.
- [21] A.Z. Khan, T.A. Kandiel, S. Abdel-Azeim, T.N. Jahangir, K. Alhooshani, Phosphate ions interfacial drift layer to improve the performance of CoFe-Prussian blue hematite photoanode toward water splitting, *Appl. Catal. B. Environ.* 304 (2022), 121014, <https://doi.org/10.1016/j.apcatb.2021.121014>.
- [22] Y.J. Guo, X.Y. Zhang, D.D. Zhang, S.L. Li, H. Wang, Y.Y. Peng, Z.Y. Bian, Catalysts containing Fe and Mn from dewatered sludge showing enhanced electrocatalytic degradation of triclosan, *Environ. Res.* 214 (2022), 114065, <https://doi.org/10.1016/j.envres.2022.114065>.
- [23] F. Rong, L. Tian, C. Feiwu, Comparing methods for predicting the reactive site of electrophilic substitution, *Acta Phys. Chim. Sin.* 30 (2014) 628–639, <https://doi.org/10.3866/PKU.WHXB201401211>.
- [24] C. Morell, A. Grand, A. Toro-Labbé, New dual descriptor for chemical reactivity, *J. Phys. Chem. A* 109 (2005) 205–212, <https://doi.org/10.1021/jp046577a>.
- [25] D. Wei, Y. Huang, J. Bai, H.J. Seo, Manipulating luminescence and photocatalytic activities of BiVO₄ by Eu³⁺ ions incorporation, *J. Phys. Chem. C* 124 (2020) 11767–11779, <https://doi.org/10.1021/acs.jpcc.0c01845>.
- [26] Y. Zhao, C. Ding, Z. Jian, W. Qin, X. Tao, F. Fan, R. Li, C. Li, A hydrogen farm strategy for scalable solar hydrogen production with particulate photocatalysts, *Angew. Chem. Int. Ed.* 59 (2020) 9653–9658, <https://doi.org/10.1002/ange.202001438>.
- [27] D. Li, Y. Liu, W. Shi, C. Shao, S. Wang, C. Ding, T. Liu, F. Fan, J. Shi, C. Li, Crystallographic-orientation-dependent charge separation of BiVO₄ for solar water oxidation, *ACS Energy Lett.* 4 (2019) 825–831, <https://doi.org/10.1021/acscenergylett.9b00153>.
- [28] W.H. Zhang, Y.Y. Peng, Y.J. Yang, L. Zhang, Z.Y. Bian, H. Wang, Bismuth-rich strategy intensifies the molecular oxygen activation and internal electrical field for the photocatalytic degradation of tetracycline hydrochloride, *Chem. Eng. J.* 430 (2022), 132963, <https://doi.org/10.1016/j.cej.2021.132963>.
- [29] Z. Wang, Y. Guo, M. Liu, X. Liu, H. Zhang, W. Jiang, P. Wang, Z. Zheng, Y. Liu, H. Cheng, Y. Dai, Z. Wang, B. Huang, Boosting H₂ production from a BiVO₄ photoelectrochemical biomass fuel cell by the construction of a bridge for charge and energy transfer, *Adv. Mater.* 34 (2022), 2201594, <https://doi.org/10.1002/adma.202201594>.
- [30] G. Wang, W. Zhang, J. Li, X. Dong, X. Zhang, Carbon quantum dots decorated BiVO₄ quantum tube with enhanced photocatalytic performance for efficient degradation of organic pollutants under visible and near-infrared light, *J. Mater. Sci.* 54 (2019) 6488–6499, <https://doi.org/10.1007/s10853-019-03316-y>.
- [31] A. Wang, J. Ni, W. Wang, X. Wang, D. Liu, Q. Zhu, MOF-derived N-doped ZnO carbon skeleton@hierarchical Bi₂MoO₆ S-scheme heterojunction for photodegradation of SMX: Mechanism, pathways and DFT calculation, *J. Hazard. Mater.* 426 (2022), 128106, <https://doi.org/10.1016/j.jhazmat.2021.128106>.
- [32] S. Lu, Y. Yu, L. Ren, X. Zhang, G. Liu, Y. Yu, Estimation of intake and uptake of bisphenols and triclosan from personal care products by dermal contact, *Sci. Total. Environ.* 621 (2018) 1389, <https://doi.org/10.1016/j.scitotenv.2017.10.088>.
- [33] Y. Xuan, B. Wang, C. Gao, K. Zhang, B. Li, M. Wang, D. Wang, J. Li, C. Lu, Substantially enhanced anti-lead poisoning performance on the CeO₂-WO₃ pairs supported by red mud: Sacrificial effect of Fe₂O₃, *Chem. Eng. J.* 450 (2022), 138165, <https://doi.org/10.1016/j.cej.2022.138165>.
- [34] Y. Liu, W. Wang, M. Si, Y. Yu, H. Zhang, (Yb³⁺, Er³⁺) co-doped TiO₂/Ag₃PO₄ hybrid photocatalyst with enhanced activity for photodegradation of phenol, *Appl. Surf. Sci.* 463 (2019) 159–168, <https://doi.org/10.1016/j.apsusc.2018.08.188>.
- [35] Z. Jiang, Y. Liu, T. Jing, B. Huang, X. Zhang, X. Qin, Y. Dai, M.H. Whangbo, Enhancing the photocatalytic activity of BiVO₄ for oxygen evolution by Ce doping: Ce³⁺ ions as hole traps, *J. Phys. Chem. C* 120 (2016) 2058–2063, <https://doi.org/10.1021/acs.jpcc.5b10856>.
- [36] N.M. Khaidukov, V.X. Quang, U.T.D. Thuy, L.D. Thanh, V.P. Tuyen, N.X. Ca, P. V. Do, Study on optical properties and upconversion luminescence of K₂YF₅:Sm³⁺ single crystals, *J. Lumin.* 237 (2021), 118201, <https://doi.org/10.1016/j.jlumin.2021.118201>.
- [37] S. Wang, P. Chen, Y. Bai, J.H. Yun, G. Liu, L. Wang, New BiVO₄ dual photoanodes with enriched oxygen vacancies for efficient solar-driven water splitting, *Adv. Mater.* 30 (2018), 1800486, <https://doi.org/10.1002/adma.201800486>.
- [38] H. Duan, H. Wu, H. Zhong, X. Wang, W. Wan, D. Li, G. Cai, C. Jiang, F. Ren, Improving PEC performance of BiVO₄ by introducing bulk oxygen vacancies by He⁺ ion irradiation, *J. Phys. Chem. C* 126 (2022) 7688–7695, <https://doi.org/10.1021/acs.jpcc.2c00433>.
- [39] Y. Hu, Y. Wu, J. Feng, H. Huang, C. Zhang, Q. Qian, T. Fang, J. Xu, P. Wang, Z. Li, Rational design of electrocatalysts for simultaneously promoting bulk charge separation and surface charge transfer in solar water splitting photoelectrodes, *J. Mater. Chem. A* 6 (2018) 2568–2576, <https://doi.org/10.1039/C7TA10361A>.
- [40] S. Wang, T. He, P. Chen, A. Du, L. Wang, In situ formation of oxygen vacancies achieving near complete charge separation in planar BiVO₄ photoanodes, *Adv. Mater.* 32 (2020), 2001385, <https://doi.org/10.1002/adma.202001385>.
- [41] Y. Zhang, Y. Huang, S.S. Zhu, Y.Y. Liu, X. Zhang, J.J. Wang, A. Braun, Covalent S-O bonding enables enhanced photoelectrochemical performance of Cu₂S/Fe₂O₃ heterojunction for water splitting, *Small* 17 (2021), 2100320, <https://doi.org/10.1002/smll.202100320>.
- [42] B. Zhang, L. Wang, Y. Zhang, Y. Ding, Y. Bi, Ultrathin FeOOH nanolayers with abundant oxygen vacancies on BiVO₄ photoanodes for efficient water oxidation, *Angew. Chem. Int. Ed.* 57.8 (2018) 2248–2252, <https://doi.org/10.1002/ange.201712499>.
- [43] B. He, S. Jia, M. Zhao, Y. Wang, T. Chen, S. Zhao, Z. Li, Z. Lin, Y. Zhao, X. Liu, General and robust photothermal-heating-enabled high-efficiency photoelectrochemical water splitting, *Adv. Mater.* 33 (2021), 2004406, <https://doi.org/10.1002/adma.202004406>.
- [44] C.S. Cao, J. Wang, X. Yu, Y. Zhang, L. Zhu, Photodegradation of seven bisphenol analogues by Bi₅O₇/UiO-67 heterojunction: Relationship between the chemical structures and removal efficiency, *Appl. Catal. B. Environ.* 277 (2020), 119222, <https://doi.org/10.1016/j.apcatb.2020.119222>.
- [45] J. Wang, X. Xu, Y. Liu, Z. Wang, P. Wang, Z. Zheng, H. Cheng, Y. Dai, B. Huang, Oxygen-vacancy-enhanced singlet oxygen production for selective photocatalytic oxidation, *ChemSusChem* 13 (2020) 3488, <https://doi.org/10.1002/cssc.202000595>.
- [46] J.M. Tobin, T.J.D. McCabe, A.W. Prentice, S. Holzer, G.O. Lloyd, M.J. Paterson, V. Arrighi, P.A.G. Cormack, F. Vilela, Polymer-supported photosensitizers for oxidative organic transformations in flow and under visible light irradiation, *ACS Catal.* 7 (2017) 4602–4612, <https://doi.org/10.1021/acscatal.7b00888>.
- [47] W.J. Chang, S. Irgen-Gioro, S. Padgaonkar, R. López-Arteaga, E.A. Weiss, Photoredox-mediated sensitization of lanthanide dopants by perovskite nanocrystals, *J. Phys. Chem. C* 125 (2021) 25634–25642, <https://doi.org/10.1021/acs.jpcc.1c06473>.
- [48] Y.J. Yang, Z.Y. Bian, Oxygen doping through oxidation causes the main active substance in g-C₃N₄ photocatalysis to change from holes to singlet oxygen, *Sci. Total Environ.* 753 (2021), 141908, <https://doi.org/10.1016/j.scitotenv.2020.141908>.
- [49] Z.H. Xie, C.S. He, H.Y. Zhou, L.L. Li, Y. Liu, Y. Du, W. Liu, Y. Mu, B. Lai, Effects of molecular structure on organic contaminants' degradation efficiency and dominant ROS in the advanced oxidation process with multiple ROS, *Environ. Sci. Technol.* 56 (2022) 8784–8795, <https://doi.org/10.1021/acs.est.2c00464>.
- [50] R. Yin, W. Guo, H. Wang, J. Du, Q. Wu, J.S. Chang, N. Ren, Singlet oxygen-dominated peroxydisulfate activation by sludge-derived biochar for sulfamethoxazole degradation through a nonradical oxidation pathway: Performance and mechanism, *Chem. Eng. J.* 357 (2019) 589–599, <https://doi.org/10.1016/j.cej.2018.09.184>.
- [51] M.P. Rayaroth, K.P. Prasanthkumar, Y.G. Kang, C.S. Lee, Y.S. Chang, Degradation of carbamazepine by singlet oxygen from sulfidized nanoscale zero-valent iron-citric acid system, *Chem. Eng. J.* 382 (2020), 122828, <https://doi.org/10.1016/j.cej.2019.122828>.
- [52] M.J. Choi, T.L. Kim, K.S. Choi, W. Sohn, T.H. Lee, S.A. Lee, H. Park, S.Y. Jeong, J. W. Yang, S.H. Lee, H.W. Jang, Controlled band offsets in ultrathin hematite for enhancing the photoelectrochemical water splitting performance of heterostructured photoanodes, *ACS Appl. Mater. Interfaces* 14 (2022) 7788–7795, <https://doi.org/10.1021/acsaami.1c18886>.
- [53] S.C. Sun, R.J. Gao, X.L. Liu, L. Pan, C.X. Shi, Z. Jiang, X.W. Zhang, J.J. Zou, Engineering interfacial band bending over bismuth vanadate/carbon nitride by work function regulation for efficient solar-driven water splitting, *Sci. Bull.* 67 (2022) 389–397, <https://doi.org/10.1016/j.scib.2021.10.009>.
- [54] S.W. Zhu, Q.G. Li, M. Huttula, T.H. Li, W. Cao, One-pot hydrothermal synthesis of BiVO₄ microspheres with mixed crystal phase and Sm³⁺-doped BiVO₄ for enhanced photocatalytic activity, *J. Mater. Sci.* 52 (2017) 1679–1693, <https://doi.org/10.1007/s10853-016-0460-0>.